COMPUTATIONS OF UNSTEADY AERODYNAMICS DUE TO BODY MOTION

T. Berglind
FOI
SE-164 90 Stockholm
Sweden

V. Brunet
ONERA
BP 72, 29 avenue de la Division Leclerc, 92322 Châtillon Cedex
France

N. Caballero Rubiato
INTA, Área de Dinámica de Fluidos
Carretera de Ajalvir, km 4, 28850 Torrejón de Ardoz, Madrid
Spain

N. Ceresola
ALENIA
Divisione Aeronautica, Corso Marche 41, 10146 Torino
Italy

R. Heinrich
DLR
Lilienthalplatz 7, 38022 Braunschweig,
Germany

S. Leicher,
EADS-M,
Military Aicraft Buisness Unit, Dept. MT63/Build. 70N, München, D-81663
Germany

B.B. Prananta
NLR
2, Anthony Fokkerweg 1006 BM, Amsterdam
The Netherlands

OVERVIEW

The research activities presented in this paper have been carried out in GARTEUR framework. Action Group AG38 started in 2001 with eight participants: Alenia, Airbus UK, DLR, EADS-M, FOI (Chairman), INTA, NLR and ONERA.
The main interest of the participants was unsteady aerodynamics due to body motion. The purpose of the activities has been to validate the participants' computational methods, to explore techniques to improve the accuracy and to develop best practise guidelines.

Computational Fluid Dynamics has had a great impact on aerospace engineering, mainly limited to steady flows, such as flow around a cruising aircraft. In some cases unsteady flow phenomena play an important role for aerodynamic features. For example gusts, passing aircrafts, flight maneuvers and buffeting cause unsteady flow. Unsteadiness in computations can occur due to moving boundaries, unsteady boundary conditions or aerodynamic instability.
Several EU-projects concerning unsteady aerodynamics have been carried out. The UNSI and TAURUS projects investigated the ability to accurately predict fluid–

structure interaction phenomena by coupling Computational Fluid Dynamics (CFD) and Computational Structural Dynamics (CSD) codes. In contrast to the UNSI and TAURUS projects, AG38 has focused merely on the unsteady aerodynamics.
Flow cases of various geometric complexities, ranging from a 2D airfoil to a realistic aircraft configuration, have been investigated. The body movement have in all the cases been oscillations in pitch.

NOMENCLATURE

c	chord
C_p	pressure coefficient
C_{pm}	mean pressure coefficient
C_{pRE}	in-phase component of C_p
C_{pIM}	in-quadrature component of C_p
C_N	normal force coefficient
f	frequency (Hz)
k	reduced frequency
M	Mach number
Re	Reynolds number
t	time
τ	dimensionless time, $\tau = \frac{2 \cdot u_\infty \cdot t}{c}$
u_∞	free stream velocity component
α	angle of incidence
α_m	mean incidence
α_0	pitch amplitude
ω	angular frequency (rad/s)

1. TIME INTEGRATION SCHEMES

In general the algorithms for computing unsteady flows are of two main types, explicit and implicit. For applications in aerospace aerodynamics, explicit methods are subject to severe stability restrictions. This often necessitates the use of allowable time steps, which are much smaller than those required to obtain accuracy, hence leading to a requirement for a large number of time steps. In addition, many of the acceleration techniques used for steady flows cannot be used, because they destroy time accuracy. An implicit time discretisation helps to bypass the time step limitations, which is especially important for the simulation of viscous high Reynolds number flows. Therefore all partners of AG38 rely on implicit methods.
For all codes used in AG38 the time derivative is discretised as a backward operator including 2 up to 4 time levels. The residual is formulated in an implicit manner for the new time level n+1 or by an average of the residuals of the new and old time levels. In general the scheme can be written as:

$$\frac{\beta_1(\underline{WV})^{n+1} + \beta_0(\underline{WV})^{n} + \beta_{-1}(\underline{WV})^{n-1} + \beta_{-2}(\underline{WV})^{n-2}}{\Delta t} + \gamma_1 \underline{R}\left(\underline{W}^{n+1}\right) + \gamma_0 \underline{R}\left(\underline{W}^{n}\right) + \gamma_{-1} \underline{R}\left(\underline{W}^{n-1}\right) = \underline{0} \quad (1)$$

$\underline{W}_i = (\rho \quad \rho u \quad \rho v \quad \rho w \quad \rho e_{tot})^T$ is the vector of conserved quantities associated to cell i, and $\underline{R}(\underline{W}_i)$ is the residual for cell i and V_i is the corresponding size of the control volume.
The selection of the coefficients β and γ influences the accuracy of the temporal discretisation. Possible values are for the coefficients are listed in TAB 1.

Time integration scheme	Order of accuracy	$\beta_1, \beta_0, \beta_{-1}, \beta_{-2}$, $\gamma_1, \gamma_0, \gamma_{-1}$
Euler Backward	first	1,-1,0,0 1,0,0
Backward difference	second	3/2,-2, ½,0 1,0,0
Backward difference	third	11/6,-3, 3/2, -1/3 1,0,0
Trapezoidal	second	1,-1,0,0 ½,½,0

TAB 1. Different options for the β and γ coefficients.

Equation (1) for the unknown $\underline{W}^{n+1}$ is nonlinear due to the presence of the term $\underline{R}\left(\underline{W}^{n+1}\right)$ and cannot be solved directly. One must therefore resort to iterative methods. All participants except INTA use the so called dual time stepping method which has been proposed by Jameson [1]. The time integration method by INTA for solving the 2D Navier-Stokes equations is the well known Beam and Warming scheme [2].

2. 2D AIRFOIL

Two AGARD test cases with a NACA0012 airfoil oscillating in pitch at transonic speed [3-7] are selected. The on flow conditions are listed in TAB 2.

	AGARD CT Case 3	AGARD CT Case 5
M_∞	0.755	0.600
Re_∞	2.50×10^6	2.44×10^6
α	0.016°	4.86°
$\Delta\alpha$	2.51°	2.44°
$k = \omega c/(2u_\infty)$	0.0814	0.0810

TAB 2. On flow conditions for the NACA0012 test cases.

The experiments are performed in the ARA 2-dimensional wind tunnel, see [3]. The common Navier-Stokes grid is depicted in FIG 1. The Navier-Stokes grid is checked to be sufficiently fine to resolve the gradients normal to the boundary layer. In both test cases the y^+-value for the first grid line is well below 1.

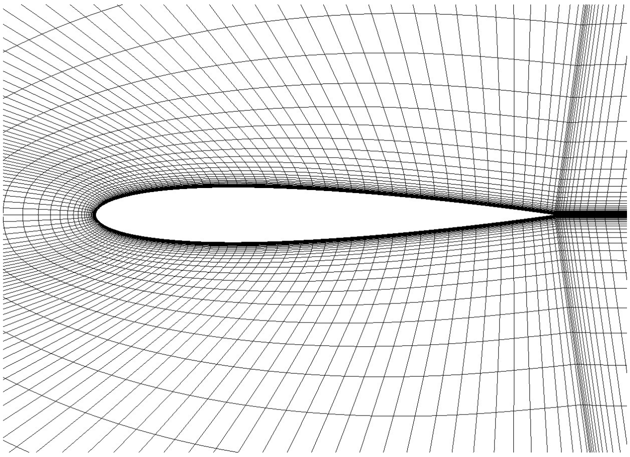

FIG 1. Common Navier-Stokes grid (193x101 = 19492 nodes).

In the first test case, a shock is moving over a substantial part of the airfoil switching from side to side. The flow remains attached throughout the cycle.
Experimental values of the pressure coefficient C_p are available at eight temporal stations. In FIG 2 the C_p –profiles for two temporal stations are plotted. There is some scatter between the computational results around the pressure peak but good agreement elsewhere. At the second station the shock in the computational results is located upstream of the shock in the experiments. However in a corresponding position with the shock on the other side of profile (temporal station 6), the agreement in shock position with experiment is good.

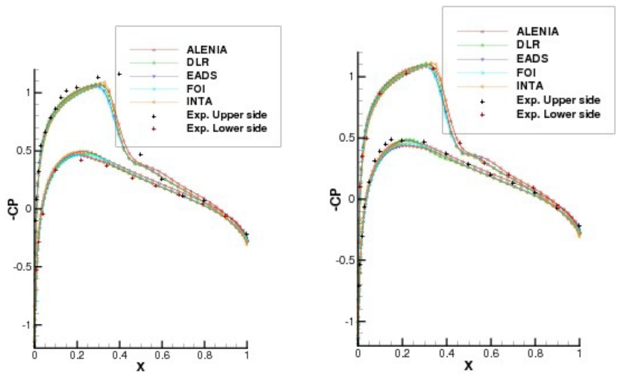

FIG 2. Pressure coefficient Cp for Navier-Stokes computations on the common grid at the temporal stations 2 and 6.

The NACA0012 is an entirely symmetric profile and the angle of attack, 0.016°, is very close to 0°. An almost symmetric solution should therefore be expected. For a symmetric case with periodic flow, the C_N-value should be symmetric around a line through origo (0., 0.).

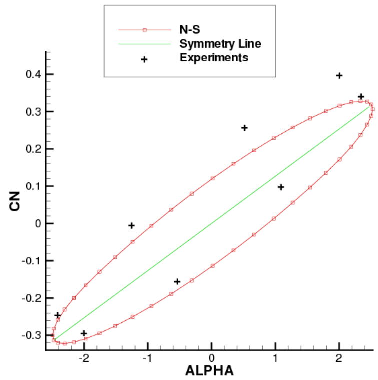

FIG 3. Comparison of the computed normal force coefficient C_N and experiments with a symmetry line.

A green line from the left turning point through origo is plotted in FIG 3. The computed values show a small deviation from the symmetry line towards the positive side which is consistent with the somewhat higher angle of attack on this side. The experimental values show a much more pronounced deviation from the symmetry line. The reasonable conclusion is that the real angle of attach must have been larger than the registered. This could possibly have been an effect of the upwash due to the sting mounting.

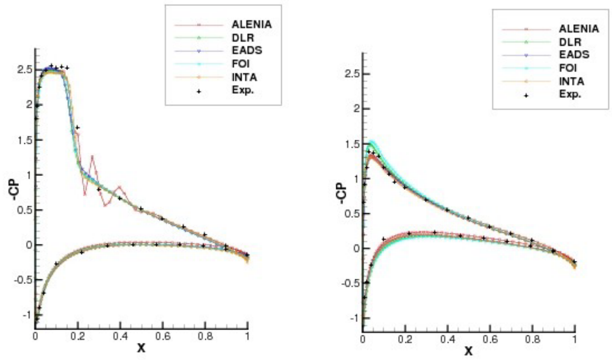

FIG 4. Pressure coefficient Cp for Navier-Stokes computations on the common grid at the temporal stations 2 and 6.

The second flow case implies a higher mean incidence, 4.86° at a somewhat lower Mach number. A shock is moving on the upper side of the wing. The flow separates with dynamic stall. In FIG 4 the C_p –profiles for the temporal stations 2 and 6, just before the turning points of the shock movement, are plotted.
In this case the shock position is in good agreement with experiments at all of the temporal stations. The agreement

between the participants' results is good except for wiggles in ALENIA's values at station 2, just downstream of the shock. This type of wiggles usually occurs if the number of sub-iterations in the dual time stepping scheme is not sufficient.
Numerous parameter investigations were performed. Comparisons of Euler, Viscous-Inviscid Interaction (VII) and Navier-Stokes solutions show that the viscous calculations in general predict shock positions and integrated forces better, especially for cases at higher angle of incidence, see FIG 5.

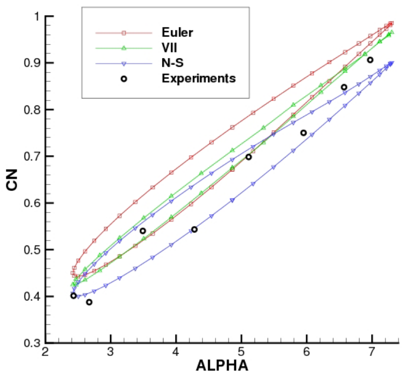

FIG 5. Comparison of normal force coefficient C_N for computations at mean incidence 4.86° with Euler, VII and Navier-Stokes computations.

Comparison of results computed on a common structured grid and an unstructured grid implied somewhat steeper shocks on the unstructured grid. This probably depends on finer grid resolution of the near field region, especially in the stream wise direction. No differences could be seen comparing results with and without GCL or comparing results with different grid moving techniques. The effect of different turbulence models had small impact on the almost symmetric case but more pronounced effects for the second test case.
In general the computed results compared well with the experimental results. At temporal stations with a shock located close to the leading edge, the computed results agree less well with experiments. This may partly be caused by transition. In the computations fully turbulent flow is assumed since no artificial boundary layer transition trips are applied in the experiments. The boundary layer at this Reynolds number probably remains laminar until the pressure peak.

3. THE LANN WING

Two transonic test cases, at 0.6° and 2.6° mean incidence were computed, see TAB 3. The LANN wing geometry is relatively simple, however especially the second case is characterised by complex flow phenomena including a shock induced separation. A good prediction of the separation as well as the shock position is still a challenging task especially for unsteady flow, see [9,10, 11]. In that context the datasets of the AGARD wind tunnel tests with the supercritical LANN wing are still an excellent basis for validation of unsteady codes.
The test cases have also been addressed within the European project UNSI [9]. Especially the test case with separation led to a large variety of results. Although there were some promising results, none of the codes could completely satisfy all aspects of the test case. So it has been found that the time has come to revisit these test cases again to see if the situation has been improved.
Within this task, Euler-boundary-layer coupling and Navier-Stokes codes have been applied to compute the flow about the pitching LANN-wing. Fourier analysed pressure distributions are compared to the experimental data available in [8].

	Case 5.1 (CT5)	Case 5.2 (CT9)
M_∞	0.82	0.82
Re_∞	7.3×10^6	7.17×10^6
α	0.6^O	2.6^O
$\Delta\alpha$	0.25^O	0.25^O
$k = \omega\, c_{root} / u_\infty$	0.204	0.206

TAB 3. On flow conditions for the selected Lann wing test cases.

The Reynolds number is based on the root chord c_{root}. The main difference between test case 5.1 and 5.2 is the mean angle of attack.
A Navier-Stokes mesh was selected from a mesh convergence study. The selected grid contains 470925 mesh points. Thereafter an Euler mesh was derived from the Navier-Stokes mesh with a reduction of 50% mesh cells corresponding to 239085 mesh points.
A time step convergence study was carried out to determine how many time steps are sufficient for accurately predicting the unsteady flow phenomena.

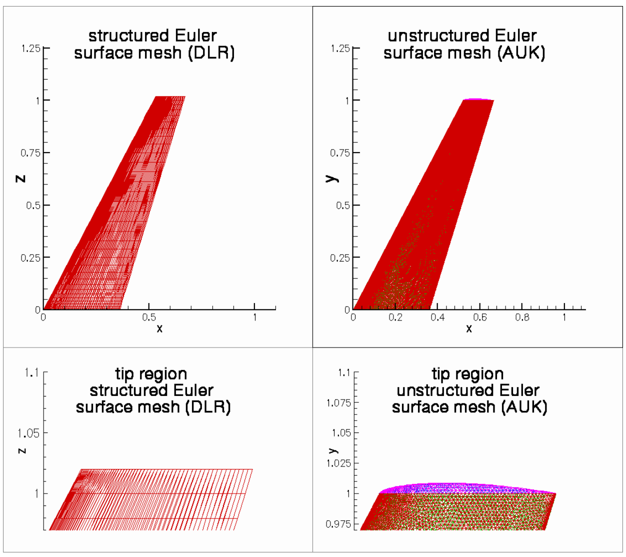

FIG 6. Surface meshes of structured and unstructured Euler-meshes.

It became clear that 25 steps are sufficient for 3rd order backward difference discretisation. For 2nd order backward discretisation 50 steps per period are sufficient.

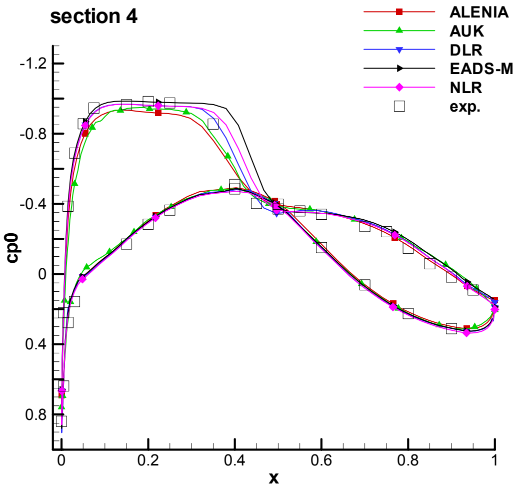

FIG 7. Averaged pressure coefficient for the LANN-CT5 at section 4.

Results of all partners at section 4 are relatively close to the experimental data, see FIG 7. The best shock position compared to the experiment is predicted by ALENIA and Airbus UK. But it should be noted, that the level of the pressure close to the trailing edge is under-predicted for both codes, which can be an indicator for a higher inherent numerical dissipation (although the number of control volumes used for the VII-code is a factor of three bigger than for the mandatory mesh used by the other partners). The results of NLR and DLR are close together, although different turbulence models have been used. It implies that this case is, as expected, less sensitive on the selection of turbulence models, because no shock induced separation occurs. On the other hand the TAU code using the SA turbulence model applied by EADS-M predicts the shock further downstream compared to DLR and NLR.

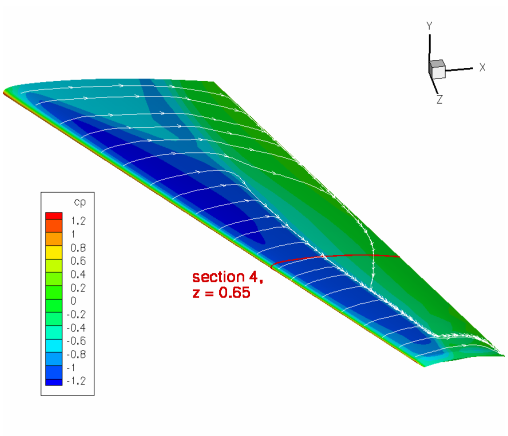

FIG 8. Pressure coefficient and stream lines for case 5.2 using FLOWer (DLR).

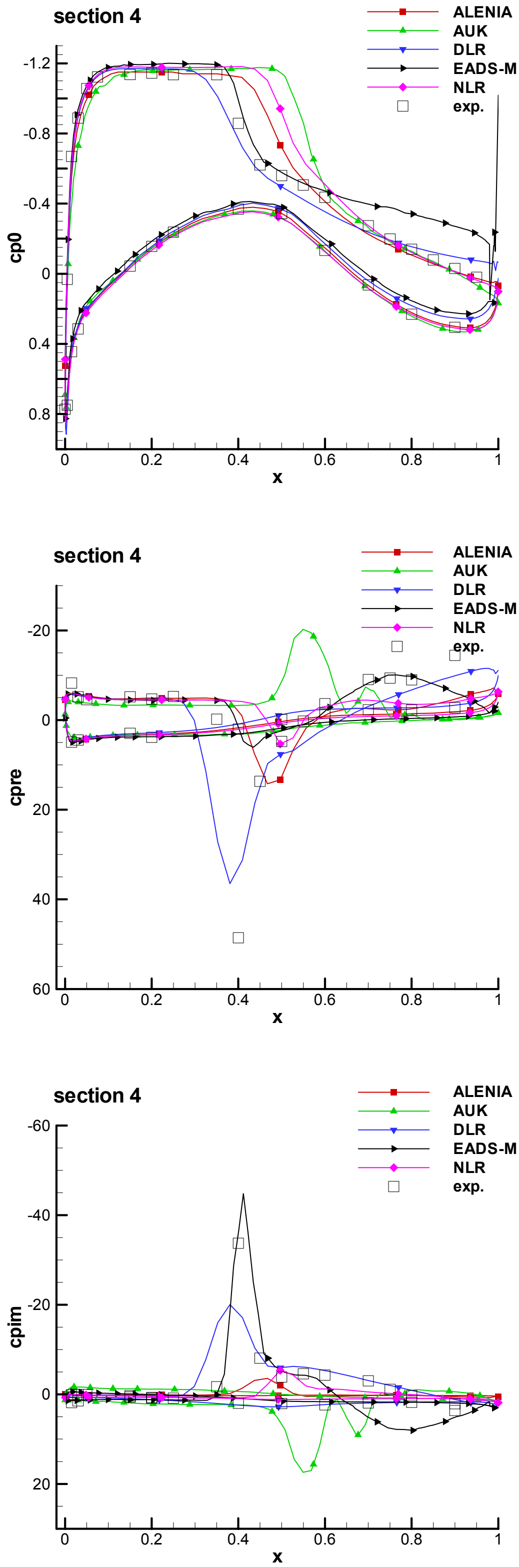

FIG 9. Averaged, real and imaginary part of pressure coefficient for the LANN-CT9 case at section 4.

The all in all best agreement is achieved by DLR using FLOWer with the kω-SST model. TAU (EADS-M) also achieves a good prediction of the shock position for the outer sections, but the pressure level behind the shock is not predicted very well (also kω-SST but on hybrid mesh). ALENIA and NLR predict the shock slightly further downstream, but the pressure level behind the shock is closer to the experimental data compared to EADS-M. In the outer part of the λ-shock the shock position is predicted furthest downstream by AUK whereas for the inner wing section the results are comparable to the other partners.

The flow case at the higher angle of incidence with shock induced separation is challenging, FIG 8. Only the more sophisticated models gave good results in this case. Results of all partners for section 4 are relatively close to the experimental data, see FIG 9. Whereas for the first test case, the flow is attached the second test case shows a separation zone behind the outer part of the λ-shock, where the two shocks coming from the root chord are joined to a shock of higher magnitude.

It can be expected, that all Navier-Stokes codes and also Euler-boundary layer coupling methods should be able to reproduce the flow pattern in this flow case.

The test cases are characterised by a viscous-inviscid interaction, which can not be captured accurately by Euler method, if computations are made for a prescribed (experimental) angle of attack. The shock position is predicted too far downstream. It is expected, that results could be improved for the first test case using a target-lift option for the steady computation (if an experimental value for the steady lift is available). The resulting angle of attack could be used as input for the following unsteady computations. However, this method will fail for the second test case, where a shock induced separation occurs.

4. OSCILLATING PARTIAL SPAN FLAP

The configuration concerns the FOI delta wing with oscillating flap. This wing was used in the measurement campaign carried out the in T1500 wind tunnel of FOI [12,13]. At section 30% and 45% of the semi-span pressure transducers are installed. Section 45% of the semi-span is usually referred to as the measurement section because it has more transducers than section 30%. The present activities concentrate on the flow region at this section. To keep the case tractable, a condition where the flow will be dominated by vortex flow, is avoided. In all cases zero angle of attack is considered.

	Test case 1	Test case 2
M_∞	0.94	0.97
Re_∞	19×10^6	19×10^6
α	0^o	0^o
δ	0^o	-8^o
$\Delta\delta$.	0.86^o	0.86^o
$k = \omega L/(2u_\infty)$	0.192	0.187

TAB 4. On flow conditions for the test cases.

The selected cases to be studied are one symmetric case (with zero flap deflection) and one asymmetric case (with 8^o flap down deflection), see TAB 4. At the selected Mach numbers, supersonic flow is formed and terminated by shockwaves. In the first case, the shockwaves are located very close to the hinge line of the flap. This situation increases the complexity of the test case, especially when the flap oscillates.

FOI generated structured multi-block grids for the computations. The grid consists of 10 blocks containing about 700,000 cells. Close to the surface, the blocks are arranged in an O-topology. These inner O-blocks are wrapped with outer blocks in a CH-topology arrangement. The finite thickness trailing edge is resolved in detail, see FIG 10. The grid points have been carefully distributed to properly capture the boundary layer profiles close to the solid surface. The typical value of y+ at the first point away from the surface is about 1.

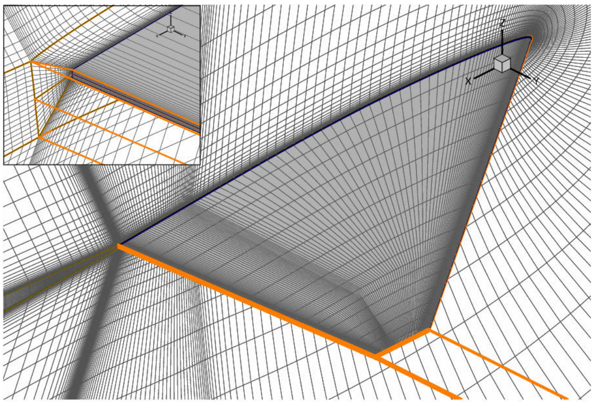

FIG 10. Structured multiblock grid around FOI delta wing, notice the detail about the trailing edge.

Comparison of Navier-Stokes results, in terms of averaged pressure coefficient, and experimental data for the first test case is presented in FIG 11.

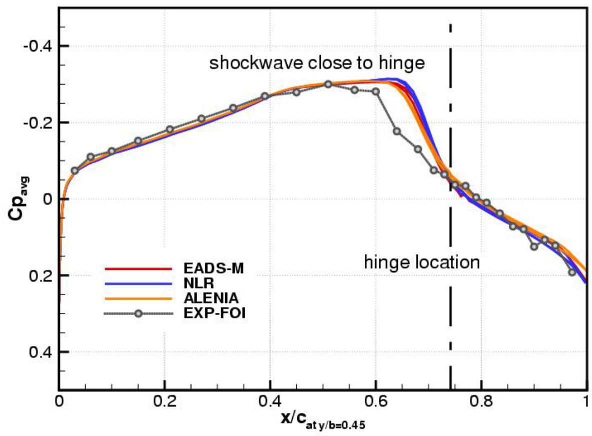

FIG 11. Comparison of experimental data and results for unsteady flow simulations based on the Navier-Stokes equations, case 1, averaged pressure coefficient.

The surface pressure coefficient is plotted as a function of the dimensionless x-position. The differences between the computational results can be clearly seen only in the neighbourhood of the shockwave. Surface pressure in front and behind the shockwave has been adequately reproduced by the computational methods. The differences in the predicted shock location and the experimental data are also visible in the real and imaginary parts of the pressure coefficient as shown in FIG 12.

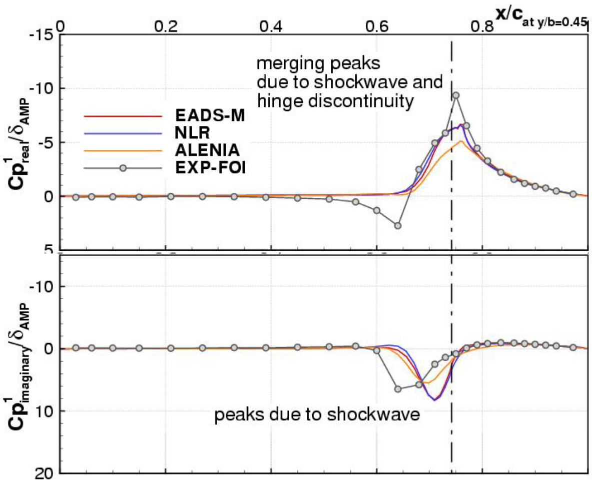

FIG 12. Comparison of experimental data and results for unsteady flow simulations based on the Navier-Stokes equations, case 1, real and imaginary pressure coefficient.

Since the shockwave is quite close to the hinge line, the peaks in the real part of the unsteady pressure are almost merged with the peaks due to hinge discontinuity. Overall agreement with the experimental data is satisfactory.

The second test case is more difficult than the first one because the incoming Mach number is higher and the flap is initially deflected 8 ° up. The components of the flow phenomena that are involved in this case can be seen from FIG 13, where the computed contours of constant pressure are shown at the measurement plane. On the surface contours of pressure coefficient is shown. The high subsonic Mach number of the incoming flow is accelerated to reach supersonic flow both at the upper and the lower side. The flap deflection creates strong camber, implying that the flow on the lower side reaches higher Mach number than on the upper side. The supersonic region at the upper side is terminated by a relatively weak shockwave well in front of the flap hinge. At the flap hinge discontinuity, the flow is therefore subsonic and creates a peak signature in the pressure as can be seen from FIG 14. The stronger supersonic region at the lower side is terminated by a strong shockwave, inducing flow separation, close to the trailing edge aft the flap hinge. The flow at the flap hinge is in this case supersonic that creates a Prandtl expansion fan. The pressure is therefore constant, see FIG 14. It is generally known that strong shockwaves are difficult to model. For the results based on Euler equations, the shockwave is too strong. Appropriate modelling should be based on Navier-Stokes equations which results in a strong shockwave-boundary layer interaction with flow separation.

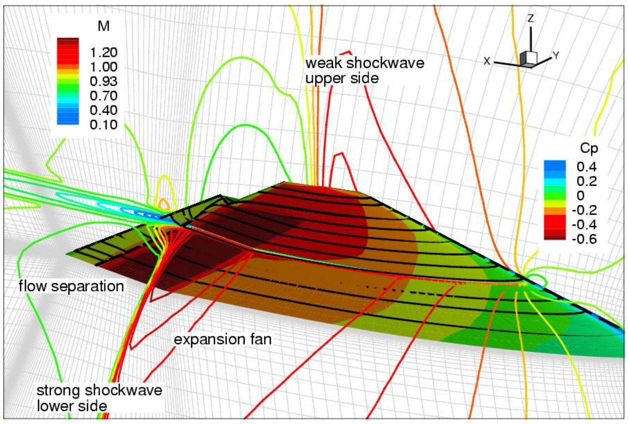

FIG 13. Mach contours of flow about the FOI delta wing at Mach 0.97, zero angle of incidence, and -8 ° flap deflection. Flow separation occurs at the foot of the shockwave.

Except for the results of ALENIA, good agreement is obtained among the computational results. It is clear that the computational methods have some difficulty in modelling the strong shockwave even with viscous flow modelling. The results of FOI, NLR and EADS-M show correct pressure level behind the shockwave but the location is too aft of the location observed in the experiment. The results of ALENIA, on the other hand, predict a correct location of the strong shockwave but the pressure level behind the shockwave indicates some problems in modelling the shockwave-boundary layer interaction (i.e. too weak). Moreover, while the weak shockwave on the upper side of the wing is predicted correctly by FOI, NLR and EADS-M, the results of ALENIA shows a discrepancy with respect to the experimental data.

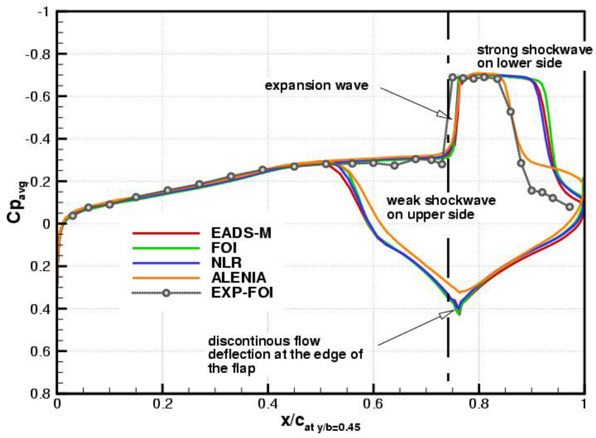

FIG 14. Comparison of the averaged pressure coefficient C_{p0} for experiments and Navier-Stokes computations. Mach 0.97, zero angle of incidence and flap deflection: $\delta\tau=-8^{o}+0.86^{o}$ sinus(0.192 τ).

In general the computational methods involved in the present test case can capture the complex flow phenomena qualitatively correctly. The global feature of the flow is determined by the interaction of these phenomena. The quantitative agreement is in satisfactory.

5. AIRCRAFT CONFIGURATION

The purpose of computing unsteady flow around a realistic aircraft configuration is to demonstrate the ability to achieve accurate flow solutions and to assess the computational efficiency. The latter is important in order to establish the usefulness of this technology to the aircraft industry.

This test case offers the opportunity to investigate flow phenomena such as shock wave boundary layer interaction, the effect of engine installation on unsteady flow characteristic, and other 3D flow features that exist in realistic aircraft configuration.

TAB 5 describes the on flow conditions for the steady state test cases. The purpose of these test cases is both to enable code-to-code validation and to that serve as initial solution to the unsteady computations.

	TC1	TC2	TC3	TC4
M_∞	0.85	0.88	0.85	0.88
Re_∞	32.5 x 10^6	32.5 x 10^6	3.09 x 10^6	3.12 x 10^6
α_m	1.5652^0	0.9542^0	1.250^0	1.0592^0
Geom.	WB	WB	WBNP	WBNP

TAB 5. On flow conditions for the steady test cases. The Reynolds number is based on the Aerodynamic Mean Chord c_{AMC}

In addition, experimental results for TC3 and TC4 are obtained from wind tunnel test performed at ARA transonic wind tunnel in Bedford – UK. The tunnel is not pressurised like ETW tunnel, hence much lower Reynolds number (compared to task 3.1 and 3.2) are simulated in this tunnel. Consequently transition locations should be properly defined.

	TC5	TC6
M_∞	0.85	0.88
Re_∞	3.09 x 10^6	3.12 x 10^6
α_m	1.5652^o	1.250^0
$\Delta\alpha$	0.50^0	0.50^0
$k_{amc} = \dfrac{\pi f c_{amc}}{U_\infty}$	0.4155	0.4155
Geom.	WBNP	WBNP

TAB 6. On flow conditions for the steady test cases.

TAB 6 describes the on flow conditions for the unsteady cases. The first case corresponds to pitching the entire aircraft about an un-swept pitch axis running through about 80% of the root chord (the exact XYZ co-ordinates of the origin of the pitching axis are 34.135, 0.0, -0.3867). In the second case the whole aircraft oscillates in pitch about 80% of the root chord (the exact XYZ co-ordinates are 30.8829, 0.0, -0.3867).

These geometries are typical large civil transport aircraft, which were supplied by Airbus UK. To avoid grid sensitivity issue on the steady and unsteady solutions, the same grids will be used for multi-block structured CFD solver (elsA (ONERA), FLOWer (EADS-M) and ENSOLV (NLR)). The VII-code used a pure tetrahedral grid. In FIG 15 and 16 grids around the aircraft configuration is depicted.

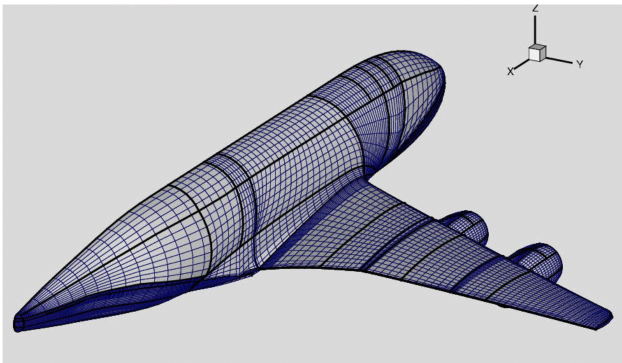

FIG 15. N39 Multi Block Structured Mesh, containing 312 blocks, 7.3 millions cells.

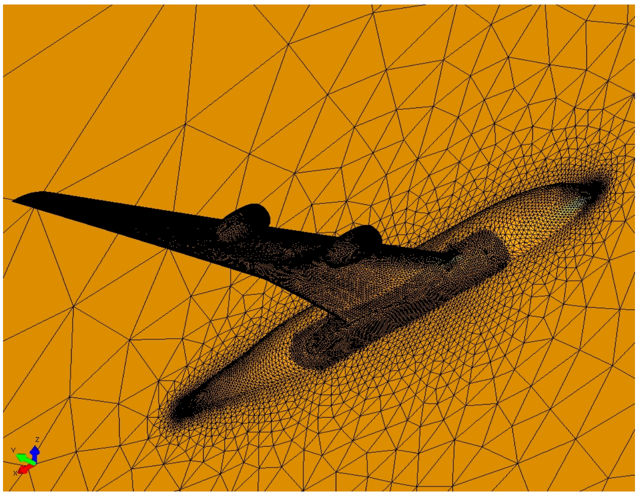

FIG 16. N39 Unstructured Mesh containing 3.62 millions tetrahedrons (627,485 nodes).

FIG 17 and FIG 18 show the surface plot of C_{pRe} and C_{pIm} respectively obtained by FLOWer (EADS-M) with LLR-kω turbulence model. It can be seen that these figures support the discussions outline in the above paragraph.

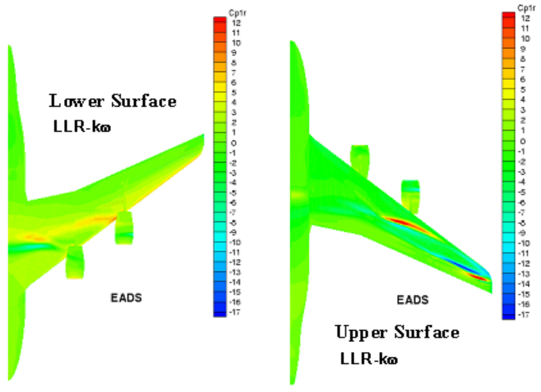

FIG 17. Surface Plot of C_p Real for a wing-body pylon configuration TC6.

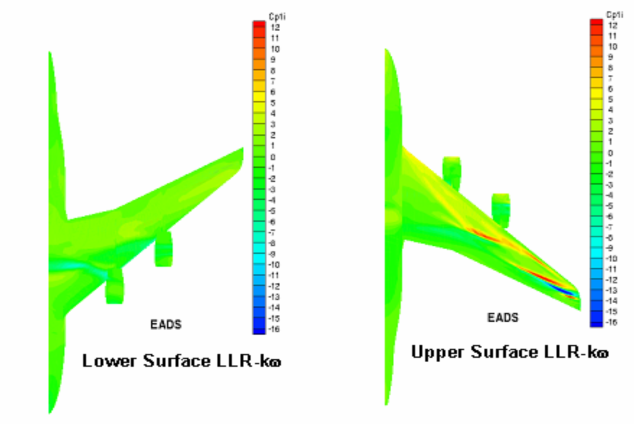

FIG 18. Surface Plot of C_p Real for a wing-body pylon configuration TC6.

In FIG 19 comparison of the participants C_{pm}, C_{pRe} and C_{pIm} values at the span station 5 (η = 47%) are plotted. The NLR and EADS results agree reasonably well. The average pressure coefficients are almost identical. The ONERA Navier-Stokes results deviate because the computations were performed without using the specified transition point data. Also the computational results from AUKs VII-code deviate from the Navier-Stokes results.

In this chapter, steady and unsteady flow computations around generic large civil transport aircraft have been performed. Cruise flow conditions around wing-body and wing-body-pylon-nacelle configurations have been simulated.

In general, pure inviscid codes are found to be inappropriate to adequately model the steady flow features and therefore are not used further in the unsteady computations. All codes that model viscous effect are shown to capture similar flow physics and simulate similar steady and unsteady flow behaviour.

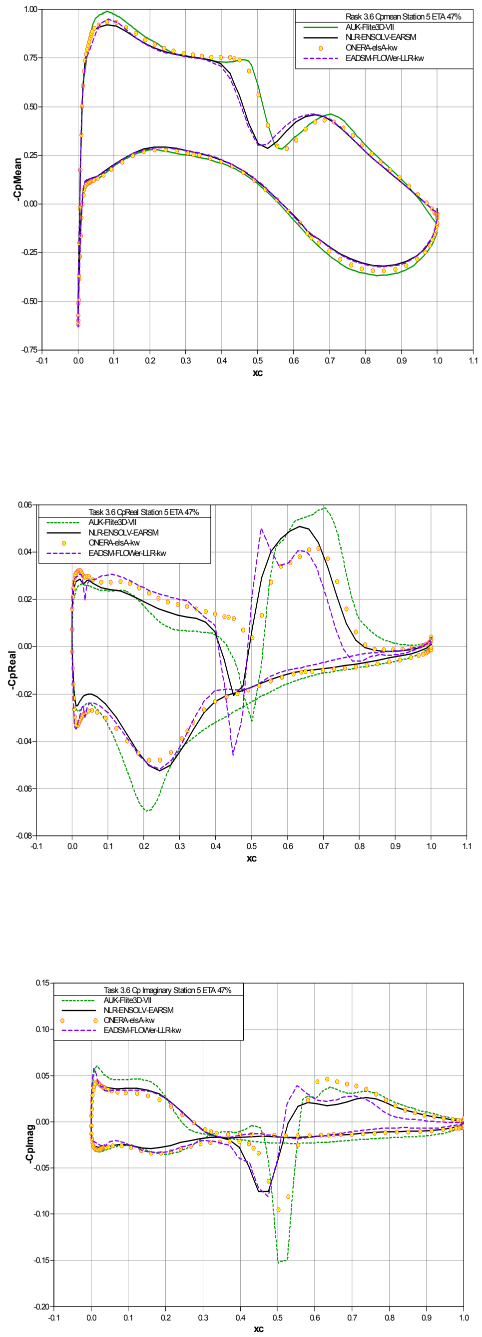

FIG 19. Comparison of span-wise C_{pm} C_{pRE}, C_{pIm} distributions for TC6 at span station 5.

6. CONCLUSIONS

For test cases treated here showing relatively weak shockwave-boundary layer interaction, methods based on the Euler and VII equations should be sufficient.

In flow cases with a relatively strong shockwave, methods based on the Reynolds-Averaged Navier-Stokes equations should be applied. An initial error in the prediction of shockwave locations would contribute to a systematic shift of forces and more importantly the moments.

In flow cases with a strong shockwave-boundary layer interaction, methods based on the Reynolds-Averaged Navier-Stokes has to be applied including a turbulence modelling which is capable of representing shockwave-induced flow separation correctly. Failure to do this, results in error in the phase lag between the aerodynamic forces and the structural motion. Example of such turbulence modelling is the k-ω SST model and the Baldwin-Barth model.

From the results obtained in the present exercise, it may be concluded that qualitatively, the CFD methods used by the AG38 partners perform satisfactorily or otherwise their deficiency can be attributed to a known aspect which can be improved.

ACKNOWLEDGEMENTS

The AG38 group is grateful to Airbus UK for supplying the geometries and experimental data for the aircraft configurations. The authors especially wish to acknowledge Dr. L. Djayapertapa at Airbus UK who made all computations with the VII-code and who has coordinated and analysed the computational results for flow around the aircraft configurations.

7. REFERENCES

[1] Jameson, A. J.: “Time dependent calculation using multigrid, with application to unsteady flows past airfoils and wings”, AIAA-paper 81-1259, 1981.

[2] Beam R.M. and Warming R.F. “An Implicit Finite-Difference Algorithm for Hyperbolic Systems in Consevation-Law Form”. Journal of Computational Physics, Vol 22, (1976).

[3] Landon R. H. (1982) "NACA0012. Oscillating and Transient Pitching", Compendium of Unsteady Aerodynamic Measurements, Data Set 3, AGARD-R-702, Aug. 1982.

[4] Woodrow, W., Hafez, M. and Osher, S. (1986) "An Entropy Correction Method for unsteady Full Potential Flows with Strong Shocks", AIAA-86-1768-CP.

[5] Batina, J. (1990) "Unstedy Euler Airfoil Solutions Using Unstructured Dynamic Meshes", AIAA-Journal, Vol. 28, No. 8, pp. 1381-1388.

[6] Eliasson, P. and Nordström J. (1995) " The Development of an Unsteady Solver for Moving Meshes", FFA TN 1995-39.

[7] Gaitonde A. L. and Fiddes S. P., “A three-dimensional moving mesh method for the calculation of unsteady transonic flows, Aeronautical Journal April, 1995, pp 150-160.

[8] Firmin M.C.P. and Mc Donald M.A., “Measurements of the flow over a low aspect ratio wing in the Mach number range of 0.6 to 0.87 for the purpose of validation of computational methods”, AGARD AR 303, 1994.G.

[9] Heinrich, R., Bleecke, H.: “Simulation of Unsteady, Three-Dimensional, Viscous Flows Using a Dual-Time Stepping Method. STAB-Tagung in Braunschweig, November 1996, in Notes on Numerical Fluid Mechanics“, Volume 60, pp. 173-180, Vieweg, 1997.

[10] Evans, J., Schwamborn, D., Weinman, K.: AGARD LANN Wing, Cases CT5 and CT9, Notes on Numerical Fluid Mechanics and Multidisciplinary Design, Vol. 81, pp. 269-278, Springer-Verlag, 2003.

[11] Zwaan, I. R. J. "LANN Wing Pitching Oscillations", Compendium of Unsteady Aerodynamic Measurements, AGARD-R-702, Aug. 1982.

[12] Karlsson A., B Winzell, Eliasson P., Nordström J., Torngren L. and Tysell L., ”Unsteady Control Surface Pressure Measurements and Computation”, AIAA-962417, 1996.

[13] Eliasson, P., Nordström, J., Torngren, L., Tysell, L., Karlsson , A. and Winzell, B., “Computations and Measurements of Unsteady Pressure on a Delta Wing with an Oscillating Flap”, Proceedings of ECCOMAS 96, 1996.